On the Seasonal and Synoptic Time-Scale Variability of the North Atlantic Trade Wind Region and Its Low-Level Clouds

MATTHIAS BRUECK,* LOUISE NUIJENS, AND BJORN STEVENS

Max Planck Institute for Meteorology, Hamburg, Germany

ABSTRACT

The seasonality in large-scale meteorology and low-level cloud amount (CC_{low}) is explored for a $5° \times 5°$ area in the North Atlantic trades, using 12 years of ERA-Interim and MODIS data, supported by 2 years of Barbados Cloud Observatory (BCO) measurements. From boreal winter to summer, large-scale subsiding motion changes to rising motion, along with an increase in sea surface temperature, a clockwise turning and weakening of low-level winds, and reduced cold-air advection, lower-tropospheric stability (LTS), and surface fluxes. However, CC_{low} is relatively invariant around 30%, except for a minimum of 20% in fall. This minimum is only pronounced when MODIS scenes with large high-level cloud amount are excluded, and a winter maximum in CC_{low} is more pronounced at the BCO. On monthly time scales, wind speed has the best correlation with CC_{low}. Existing large-eddy simulations suggest that the wind speed–CC_{low} correlation may be explained by a direct deepening response of the trade wind layer to stronger winds. Large correlations of wind direction and advection with CC_{low} also suggest that large-scale flow patterns matter. Smaller correlations with CC_{low} are observed for LTS and surface evaporation, as well as negligible correlations for relative humidity (RH) and vertical velocity. However, these correlations considerably increase when only summer is considered. On synoptic time scales, all correlations drop substantially, whereby wind speed, RH, and surface sensible heat flux remain the leading parameters. The lack of a single strong predictor emphasizes that the combined effect of parameters is necessary to explain variations in CC_{low} in the trades.

1. Introduction

Low-level clouds dominate the subtropical oceans (Warren et al. 1988), especially in regions where the large-scale vertical motion is subsiding. Stratocumulus is found over the eastern ocean basins where pronounced subsidence combined with cold sea surface temperature (SST) maintains a high stability in the lower troposphere. Deeper into the tropics, where subsidence is less pronounced, the ocean surface is warmer, and the stability is decreased, and broken fields of shallow cumulus in deeper boundary layers are more ubiquitous (Stevens 2005).

Both stratocumulus and shallow cumulus are crucial to the Earth's radiative balance, because they act to cool the Earth system by reflecting shortwave radiation (Hartmann et al. 1992). How those radiative effects might change with global warming has received increasing attention, since the representation of marine low-level clouds has been shown to dominate the spread in climate sensitivity (Bony and Dufresne 2005; Vial et al. 2013). These uncertainties ultimately relate to the difficulty of parameterizing low-level clouds in global climate models and coupling them to the large-scale flow (Boucher et al. 2013). To advance parameterizations and our understanding of climate change, more insight into how marine low-level clouds interact with their large-scale environment is thus needed.

Efforts to do so are generally challenged by the sparseness of observational records over open oceans. Nevertheless, using radiosonde and surface measurements from ocean weather stations and ships, sometimes combined with model reanalysis data, early studies have laid the basis for much of our current understanding of clouds and their relationship to the environment (Slingo 1987; Klein and

---

* Current affiliation: Universität Leipzig, Leipzig, Germany.

Corresponding author address: Louise Nuijens, Max Planck Institute for Meteorology, Bundesstrasse 53, 20146 Hamburg, Germany.
E-mail: louise.nuijens@mpimet.mpg.de

Hartmann 1993; Bretherton and Pincus 1995; Klein et al. 1995; Klein 1997). These studies have recently been strengthened by observations from advanced remote sensing platforms in space [e.g., the International Satellite Cloud Climatology Product (ISCCP), the Moderate-Resolution Imaging Spectroradiometer (MODIS), PATMOS-x, *CloudSat*, and *CALIPSO* (Mauger and Norris 2010; Myers and Norris 2013; Li et al. 2014)]. Well established are those relationships between low-level (stratiform) cloud amount and the lower-tropospheric stability (LTS), which measures the difference between the potential temperature at 700 hPa and the surface (Slingo 1987; Klein and Hartmann 1993; Wood and Bretherton 2006). LTS, and variations thereof, has been used in the parameterization of low-level cloud cover (Slingo 1987) and is probably the most widely used parameter today to separate broken cumulus fields from more persistent high-cloud-cover stratocumulus fields within regions of mean subsiding motion (Medeiros and Stevens 2011). Other parameters of importance are the relative humidity (RH) at the cloud level (Slingo 1987; Bretherton and Pincus 1995), and the amount of cold-air advection and surface wind speed (Klein 1997). All of these have been found to increase subtropical low-level cloud amount as they increase. Changes in subsidence have also been found to correlate with cloudiness, both directly, by pushing down the top of the cloud layer, and indirectly, by altering the inversion strength (Klein et al. 1995; Myers and Norris 2013).

The majority of such studies have focused on changes in cloudiness in the stratocumulus regime or on changes in transition regions where stratocumulus begins to break up and shallow cumuli are developing underneath (Bretherton and Wyant 1997; Sandu et al. 2010). In contrast, those regions with predominantly trade wind cumuli, the fair-weather regimes in the downstream trades, lack such detailed studies. Reasons for this may be the small number of field studies conducted in that region, the fact that satellite sensors did not have the footprint needed to accurately observe small cumuli, or simply because stratocumulus, with its much higher cloud amount, has been considered of greater importance. As such, our understanding of what drives the variability in trade wind cloudiness is less developed. Perhaps as a result, the spread in predicted low-level-cloud feedback among climate models is especially large here (Bony and Dufresne 2005; Medeiros and Stevens 2011). And because the fair-weather trades cover such large regions over subtropical and tropical oceans, giving them a large statistical weight, the uncertainty in cloud feedback has far-reaching effects [e.g., on climate sensitivity (Vial et al. 2013)].

In improving parameterizations for climate models and numerical weather prediction, an important question is the time scales at which variability in cloudiness is pronounced, and thus, the time scales at which the parameterizations need to act. Much of the previously mentioned studies address relationships on monthly or longer time scales. However, Klein (1997) noted that most correlations between cloud amount and environmental parameters decrease when monthly means are removed. Strikingly, on daily time scales, no single parameter could explain more than 13% of the variance in cloud amount. Mauger and Norris (2010) emphasized that whereas thermodynamic controls on cloud amount such as LTS or SST act on longer time scales, dynamic controls such as the large-scale vertical motion may exert a dominant control on shorter time scales.

That more than a single predictor is needed to explain variations in cloudiness also emerges in recent large-eddy simulations used to study the response of stratocumulus and shallow cumulus–topped boundary layers to a warming climate (Bretherton et al. 2013). Important parameters, such as subsidence, free-tropospheric humidity, inversion stability, wind speed, or aerosols, change cloud amount in different ways. Because these parameters are correlated, the combined effect of all of them needs to be considered in order to understand changes in clouds into a different climate.

In this work, the seasonal cycle in low-level cloudiness and its large-scale flow is explored specifically for a typical trade wind region. Furthermore, it is evaluated if relationships that act on seasonal time scales are also important for variability in cloudiness on shorter synoptic time scales. The region chosen is located over the western North Atlantic, upstream of the Barbados Cloud Observatory (BCO), which is a remote sensing site located on the eastward tip of Barbados. As shown by 2 years of BCO data, trade wind cloudiness, from clouds with tops below 5 km, has a relatively small seasonal cycle around a mean value of about 30%. The relatively small seasonal cycle is because cloud amount from clouds below 1 km [near the lifting condensation level (LCL)] is relatively invariant over longer time scales and contributes the larger part (two-thirds) to total cloud amount (Nuijens et al. 2014). The other one-third contribution comes from clouds present at heights above 1 km, and especially the presence of stratiform outflow near the detrainment level of cumulus tops, just below the trade wind inversion. This component is more frequent during boreal winter.

The periods with more stratiform outflow are often periods during which clouds are, on average, deeper and larger and produce more warm rain. A hypothesis of why this stratiform outflow is more common during

winter is that shallow convection at that time is more vigorous, related to the larger surface fluxes in that season. The presence of warm rain and mesoscale organization also supports larger and deeper clusters of clouds that detrain sufficient moisture near the inversion to form extended stratiform layers. Although summer is warmer, shallow convection may be suppressed because of the presence of nearby deep convection and its associated surrounding downward motion.

Beyond the BCO observations, this study uses the longer MODIS satellite record, combined with ERA-Interim, to study relationships of cloudiness with the large-scale flow. This allows us to assess whether the seasonality observed at the BCO is present in a broader trade wind region over a period longer than 2 years. The measurements at the BCO, in turn, help evaluate how MODIS performs and whether its measurements are biased when layers of high cirrus clouds occur. In section 2, our data and methods are introduced, and a brief overview of the BCO is provided. Section 3 first describes the seasonality of the boundary layer structure in the North Atlantic and reveals the associated variability in low-level cloudiness from ground-based and satellite-borne observations. Section 4 discusses the relationships between cloud amount and its environment on seasonal and synoptic time scales. Conclusions follow in section 5.

2. Data and methods

We use 12 years of data from ERA-Interim (2000–2012) to study the large-scale meteorological situation over the subtropical North Atlantic Ocean for a $5° \times 5°$ area upstream of Barbados (10.5°–15.5°N, 54°–59°W). The 12-yr climatology of cloudiness is derived from the passive remote sensing MODIS instrument aboard the *Aqua* and *Terra* satellites. Ground-based lidar measurements performed at the BCO are used to evaluate cloudiness during the years 2010–12.

a. The MODIS cloud product

To derive cloudiness, the MODIS level-2 MOD06 cloud product is used (Platnick et al. 2003; King et al. 2003). Only daytime overpasses are used, at 1430 (*Terra*, descending) and 1730 UTC (*Aqua*, ascending), because the visible channels provide additional confidence in the retrievals. The horizontal resolution of the MOD06 product is 1 km at nadir and decreases away from nadir. With increasing sensor zenith angle, clouds are increasingly observed from their sides rather than from their tops, which leads to an overestimation of cloud amount. For this reason, all data with a sensor zenith angle greater than 45° are discarded. We regrid the data from the original curvilinear to a rectilinear grid of 0.05°

in both the latitudinal and longitudinal directions using a conservative bilinear interpolation method. Each 0.05° grid point then contains 25 pixels at the original 1-km resolution, with 25 cloud-mask values that are used to derive cloud cover. The cloud mask can take four values to indicate the confidence of a pixel containing cloud: clear, probably clear, probably cloudy, and cloudy (Frey et al. 2008; Ackerman et al. 2008). In this work, only the number of cloudy pixels is used, thus adopting a more conservative estimate.

The cloud-top pressure (CTP) product that is derived by CO_2 slicing [for a detailed description, see Platnick et al. (2003); Menzel et al. (1983)] is used to identify low-level clouds, defined here as those clouds with a CTP larger than 550 hPa (roughly 5 km above mean sea level, and near the melting level). This definition includes somewhat deeper clouds than the low-level cloud category from ISCCP, which uses a threshold of 680 hPa. However, cumulus clouds as deep as 4 km are not infrequent near Barbados (Nuijens et al. 2014). High-level clouds are identified as those clouds with a CTP less than 440 hPa, following the ISCCP definition.

It is not unusual to find grid points with high-level clouds that are directly surrounded by low-level clouds. This halo of low-level clouds surrounding high-level clouds is likely a result of the CO_2 slicing method in cases of broken cloudiness, the effect of which is to increase the apparent CTP. As a result, the low-level cloud amount from MODIS exhibits a clear positive correlation with high-level cloud amount, a correlation that is absent in the ground-based lidar observations (not shown). Because high-level cirrus clouds in this region are advected by upper-level westerlies, whereas the low-level cloud field is advected by the easterly trade winds, the correlation cannot be explained by the properties of the underlying air mass in which the clouds form. Although other physical mechanisms for such a correlation can be imagined, we assume that the signal is spurious and remove these halo points. This may lead to an underestimation of high-level cloud amount, but this shortcoming is accepted, given that our focus is on low-level clouds.

The cloud cover from high-level clouds (CC_{high}) and low-level clouds (CC_{low}) for each *Terra* and *Aqua* scene is derived simply by averaging the cloud cover of individual 0.05° grid points, but only for those scenes that meet the following criteria. First, the MODIS swath (for zenith angles less than 45°) must cover more than 50% of the $5° \times 5°$ area upstream of Barbados defined above. Scenes with a smaller swath coverage are set to missing value. Second, because high-cloud occurrence effectively reduces the area over which CC_{low} can be calculated, scenes must have a CC_{high} less than 20%; otherwise, CC_{low}
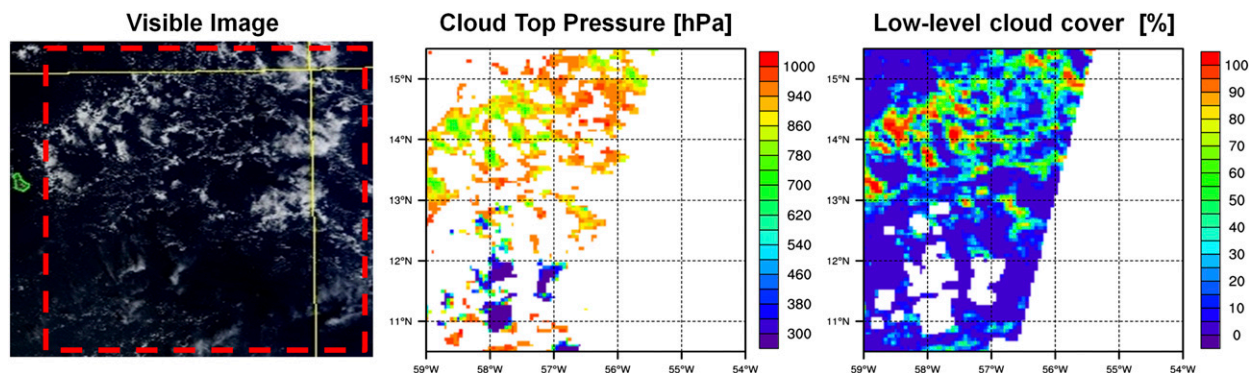
FIG. 1. (left) MODIS visible image from the daytime *Terra* overpass within the 5° × 5° area upstream of Barbados (red dashed box). Barbados is at the left side (green border). (middle) Cloud-top pressure of grid points with MODIS-swath zenith angles less than 45°. (right) Low-level cloud cover (clouds below 550 hPa).

will be assigned a missing value. The subjective choice for these specific thresholds provides the best agreement between CC_{low} from MODIS and from ground-based lidar instruments (see also section 3).

The procedure for calculating CC_{low} is illustrated in Fig. 1. The left panel shows the visible MODIS image for the daytime *Terra* overpass on 1 February 2011. The CTP and cloud cover for grid points that are within the swath, at zenith angles less than 45°, are shown in the middle and right panels. The swath-to-area ratio in this example is 59.6%. Those grid points with a CTP less than 550 hPa are masked in the right panel. The remaining area (53.6%) is used to derive CC_{low}, which here equals 21.3%.

The total dataset spans the period from March 2000 to June 2012 and includes 3198 *Terra* scenes and 2521 *Aqua* scenes. After applying the above criteria, the number of scenes is reduced to 1375 and 1110, respectively (Table 1). When both sensors are combined, 1713 days are left with a cloud cover estimate, sometimes from either *Terra* or *Aqua*, and sometimes from both.

b. Ground-based lidar data

To derive cloud cover at the BCO, 2 years of Raman lidar and laser ceilometer data are used. The BCO is a state-of-the-art remote sensing site located on the eastern coast of Barbados, directly facing the Atlantic Ocean, and in operation since 1 April 2010 (Nuijens et al. 2014). Cloud cover from the ceilometer and lidar is derived by dividing the number of vertical profiles with cloud by the total number of profiles, providing a temporal cloud cover.

The ceilometer measures backscatter from cloud droplets at the 1064-nm wavelength. Only returns up to 5 km are used, where signal-to-noise ratios are reasonable. A gradient method that is insensitive to changes in solar background light is used to derive the first detected

cloud-base height at any height below 5 km, which contributes to CC_{low}. Periods with rain are excluded. Although the ceilometer is less powerful than the Raman lidar, it suffered less downtime during the 2-yr period and has both higher temporal resolution (30 s) and vertical resolution (15 m). The higher temporal resolution is found to have a significant influence on the derived cloud cover, because it allows a better detection of patches of decaying clouds at heights beyond the lifting condensation level, which are otherwise smeared out in the averaging procedure of the lidar (Nuijens et al. 2014).

The lidar measures backscattered energy at three wavelengths (1064, 532, 355 nm), which is averaged to a 2-min resolution every 60 m up to 15 km. Because the lidar is more powerful, it is used to derive CC_{high}, which is defined as the fraction of profiles with cloudy returns anywhere above 6.9 km, roughly 440 hPa. Returns are identified as cloudy when the particle backscatter coefficient β at 532 and 355 nm exceeds 30 Mm^{-1} sr^{-1}, and the error in β_{355} and β_{532} is less than 30%. Single isolated cloudy pixels that are likely noise are excluded. The lidar hatch closes for 1 h (1530–1630 UTC) when the sun is directly overhead and during periods of rain (Nuijens et al. 2014).

Humidity and temperature profiles are measured with the Raman lidar as well, but only from 1 April 2011 to 1 April 2012. By measuring backscattered energy at the shifted Raman frequency in the UV spectral range at 355 nm, the concentration of water vapor is derived. Furthermore, by making use of the pure rotational Raman spectra (PRRS) technique, air temperature is derived (Serikov and Bobrovnikov 2010). The profiles of humidity and temperature are only available during nighttime, when there is no interference of background solar light, between 0000 and 0800 UTC (between 2000 and 0400 local time). To achieve enough accuracy, the

TABLE 1. Number of daytime *Terra* and *Aqua* scenes and days (*Terra* and *Aqua* combined) between March 2000 and June 2012 in the Barbados upstream area (10.5°–15.5°N, 54°–59°W), dependent on the two quality criteria (see text).

	Terra	*Aqua*	Days
No filter	3198	2521	—
Coverage > 50%	2195	1780	—
Coverage > 50%, $CC_{high} < 20\%$	1375	1110	1713

raw data are averaged into 2-min profiles for water vapor and 1-hr profiles for temperature, available at a 60-m resolution up to 15 km.

c. ERA-Interim

The ERA-Interim product is based on the Cy31r2 version of the Integrated Forecast System (IFS) (Simmons et al. 2007). The horizontal resolution (N128) of the quasi-regular Gaussian grid is approximately 0.7° at 10°N. The vertical resolution is 61 model levels, with a pressure difference that increases from 4 hPa in the lowest levels to 40 hPa at a pressure of 440 hPa. The profiles of temperature, humidity, and the three wind components are averaged over the 5° × 5° region upstream of Barbados. Additional products used are the SST; the LTS, which is the potential temperature difference $\theta_{700\_hPa} - \theta_{1000\_hPa}$; the wind shear, here defined as the wind speed difference between 700 and 900 hPa; the sensible and latent heat fluxes (SHF and LHF, respectively); and the temperature advection T_{adv}. The latter is derived by multiplying the near-surface wind speed (wspd) and wind direction (wdir) by the near-surface temperature difference over a distance of 5°. Only the daytime (1200 and 1800 UTC) data are used, in agreement with using only the daytime MODIS overpasses.

Although ERA-Interim has not been used extensively for studies that assess relationships between marine boundary layer clouds and large-scale meteorology, its predecessor, ERA-40 has been used for such purposes—for instance, for estimates of boundary layer height (Stevens et al. 2007; Teixeira et al. 2011). Through the implementation of the eddy-diffusivity mass flux approach (Köhler 2005; Teixeira et al. 2011) in ERA-Interim, the boundary layer structure has further improved. A good agreement between ERA-Interim and independent radiosondes released from research vessels across the Atlantic has been found, both in terms of the mean boundary layer structure and its variability (von Engeln and Teixeira 2013). Not only boundary layer height, but also low-level cloud-top pressure in the ECMWF model, has been found to agree well with space-borne estimates along another
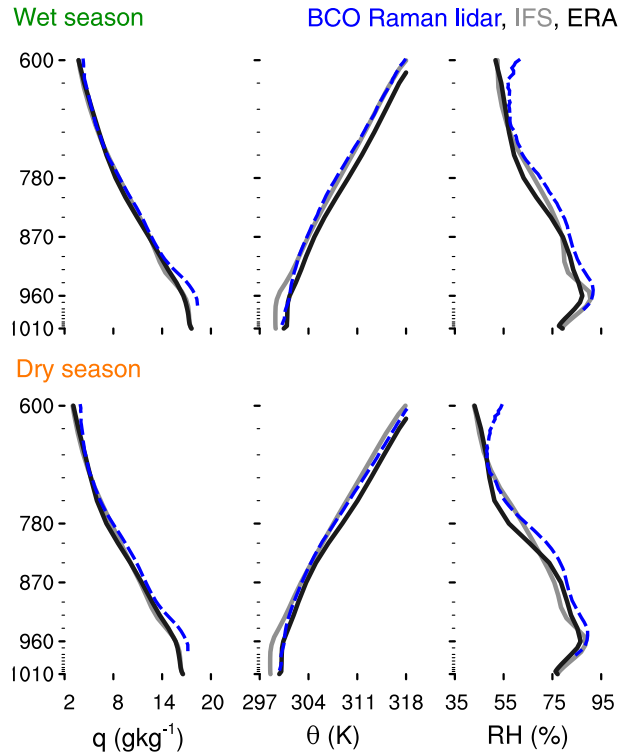

FIG. 2. Lower-tropospheric profiles of BCO Raman lidar, ERA-Interim, and the ECMWF IFS for April 2011–April 2012. The mean structure of (left) specific humidity, (middle) potential temperature, and (right) relative humidity for (top) the wet and (bottom) the dry seasons is shown.

typical trade wind trajectory in the Pacific (Karlsson et al. 2010).

A comparison of the boundary layer structure near Barbados in ERA-Interim with that in the operational version of the model, the ECMWF IFS, and in the BCO observations (the Raman lidar temperature and humidity profiles) is shown in Fig. 2. The comparison is done for the period from April 2011 to April 2012, for which Raman lidar measurements are available. The IFS data include 3-hourly forecasts for an area of about 75 km × 45 km upstream of Barbados (13.14°–13.42°N, 58.5°–59.06°W). The forecasts are initialized from 1200 UTC on the previous day, using just the 12–36-h integration period to get the forecast for 0000–2100 UTC. Only the lowest 31 levels are used, reaching from 10 to 7600 m, with an interval of approximately 20 m at level 1 and approximately 500 m at level 31.

Average humidity, temperature, and relative humidity profiles are computed for the dry and the wet seasons. The averaging is not performed layer by layer; hence, gradients such as the trade wind inversion are more smoothed in the averaged profiles in Fig. 2 than in individual profiles. This is especially true because the height of the inversion layer, or the maximum gradient

in the virtual potential temperature, is observed to be highly variable, ranging between 1.5 and 4 km (not shown). However, from the relative humidity profile, the location of the average inversion can be identified between 840 and 780 hPa in ERA-Interim and between 810 and 850 hPa in the BCO data. It is somewhat less pronounced in the IFS, which may be related to the short integration period, which may distort the structure of the inversion if the latter needs a longer time to develop. The 30-hPa shift between the BCO and ERA-Interim is likely due to the different locations of the data sources, whereby the BCO is downstream of the 5° × 5° area over which the ERA-Interim profiles are derived. Over the pass-through period, clouds and convection may have deepened the boundary layer. Other differences include the absolute humidity and temperature below 900 hPa, whereby the large humidities from the lidar have been verified with airborne in situ measurements upstream of Barbados. From a model point of view, a dry bias within the lower layers is not fully understood but may relate to the model being too efficient at vertical moisture mixing.

Despite the differences in boundary layer depth and humidity, the overall structure of the boundary layer is reasonably represented by ERA-Interim, including evidence of the transition layer just above 960 hPa, which is a smaller inversion that is typically found near cloud base. Most importantly, the model reproduces the main changes in boundary layer structure from the dry season to the wet season, including the weakening of the trade wind inversion and the increase in relative humidity above 870 hPa. The ECMWF IFS, especially in longer integrations, has also been found to perform very well in reproducing robust features of trade wind cloudiness, in strong contrast to a large number of climate models (not shown).

Last, we evaluated the agreement between the surface sensible and latent heat fluxes from ERA-Interim with those of the climatology of the Hamburg Ocean Atmosphere Parameters and Fluxes from Satellite Data (HOAPS 3.2) set, which is based on SSM/I passive microwave radiances (Fennig et al. 2012), and found a good correlation between the two datasets. However, given the biases in modeled temperature and humidity at low levels [e.g., below cloud base and near the surface (Fig. 2)], the surface fluxes must be interpreted with some caution.

3. Seasonality

a. Atmospheric structure and large-scale forcings

The region upstream of Barbados experiences two distinct seasons, which are closely tied to the location of the intertropical convergence zone (ITCZ). During Northern Hemisphere winter, the ITCZ is located well south of
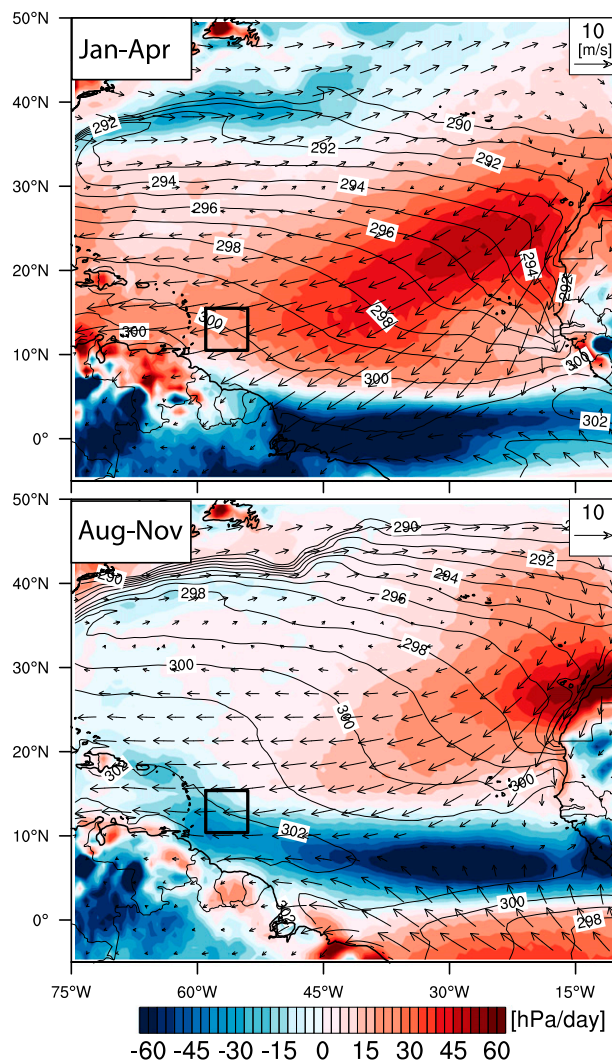

FIG. 3. Climatological pattern of large-scale vertical velocity ω_{700_hPa}, sea surface temperature, and near-surface winds, from 12 years of ERA-Interim data (2000–12). Isolines represent the SST (1-K spacing for SST > 290 K); colored contours show ω_{700_hPa} ($\omega > 0$ hPa day^{-1} implies subsiding motion), and vectors represent the wind speed and wind direction at 1000 hPa (10 m s^{-1}). The black box indicates the 5° × 5° area upstream of Barbados over which ERA-Interim and MODIS data are analyzed.

Barbados, and conditions near Barbados are typical for trade wind regimes. Moderate large-scale subsidence is present, and a trade wind inversion is located near 800 hPa, evident in both the RH and potential temperature profile (Figs. 3 and 4). Fairly strong easterly to northeasterly winds advect relatively cold and dry air from regions farther upstream (Fig. 4). The wet season starts near the end of May and early June, when the large-scale vertical motion abruptly changes to moderate mean upward motion as the ITCZ migrates northward. Barbados is then located on the edge of the ITCZ and experiences weaker winds that come
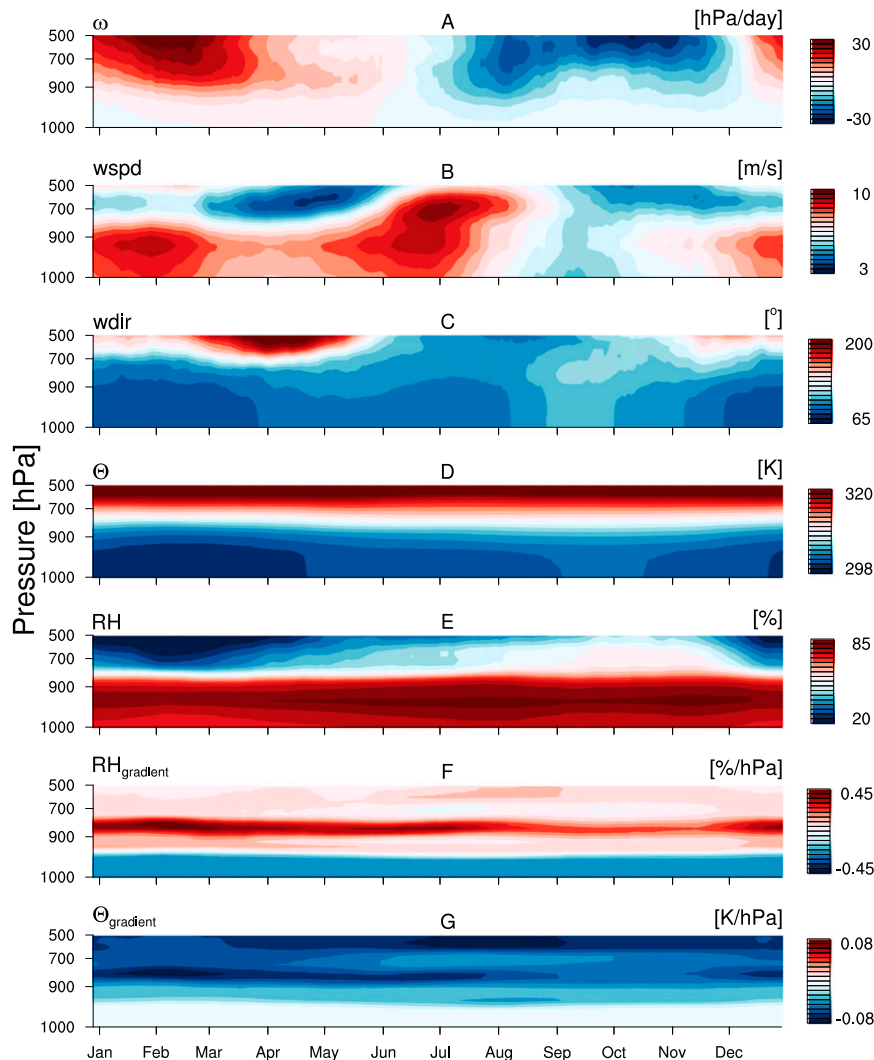
FIG. 4. Seasonal cycle in the vertical structure of monthly means (a) large-scale vertical velocity, (b) wind speed, (c) wind direction, (d) potential temperature, (e) relative humidity, (f) gradient in relative humidity, and (g) gradient in potential temperature. Monthly means of ERA-Interim data from 2000 to 2012 averaged over the 5° × 5° area upstream of Barbados shown in Fig. 3.

from the east, sometimes even slightly from the southeast, and the layer over which those easterly winds prevail is deeper. The air masses advected into the region are warmer and more humid, and especially in late summer (after August) the trade wind inversion is less well defined (Figs. 3 and 4).

One noteworthy deviation from these two marked regimes is the seasonality in the wind speed, which does not only maximize during the winter months, but has a second maximum from June to July (Fig. 4), which is often called the Caribbean low-level jet. It has a similar but even more pronounced seasonality within the Caribbean Sea (Small et al. 2007; Muñoz et al. 2008) and coincides with an increase of the surface pressure gradients as the North

Atlantic subtropical high extends farther westward (Kelly and Mapes 2011; Muñoz et al. 2008).

The distinct seasons, with either moderately subsiding motion ($\omega > 0\,\mathrm{hPa\,day}^{-1}$) or moderately rising motion ($\omega < 0\,\mathrm{hPa\,day}^{-1}$), make this region particularly interesting for climate modeling studies. In climate models, regions with low-level clouds, identified as those where $\omega_{500\_\mathrm{hPa}}$ or $\omega_{700\_\mathrm{hPa}} > 10\,\mathrm{hPa\,day}^{-1}$, are found to be a major source of the uncertainty in cloud feedbacks and climate sensitivity. However, low-level clouds, such as trade wind cumuli, occur not only in regions with mean subsiding motion, but also in between periods of deeper convection. Hence, the periods with mean rising motion during the wet season

offer an opportunity to extend the typical trade wind conditions to conditions for which we have not observed and modeled the behavior of trade wind cumuli very well. Even during the dry season, ω near Barbados reaches, on average, only $30\,hPa\,day^{-1}$, which is less than what has been typically found in past field campaigns and what is typically prescribed in modeling studies. For instance, modeling studies based on the Barbados Oceanographic and Meteorological Experiment (BOMEX) prescribe $50\,hPa\,day^{-1}$ (Siebesma et al. 2003), and the Rain in Cumulus over the Ocean (RICO) modeling study prescribes $40\,hPa\,day^{-1}$ (Van Zanten et al. 2011).

If we use the profiles in Fig. 4 to derive parameters that have been related to cloudiness in past studies, such as the LTS and the relative humidity in the boundary layer at 850 hPa, we find that their seasonality, along with seasonality in low-level cloud amount CC_{low}, does not simply follow the relationships that emerged from previous work (Fig. 5). Instead, parameters, such as the wind speed and the surface latent heat flux, appear as (additional) important factors that may explain the seasonality in cloudiness.

The LTS is a parameter that is often used to further separate broken cumulus cloud fields from overcast stratiform cloud fields within regions of subsiding motion (Klein and Hartmann 1993). It is typically between 12 and 14 K upstream of Barbados, with a minimum of 12 K in September–October (Fig. 5d). Those values are on the lower end of the Klein and Hartmann (1993) relationship that predicts cloud cover as a function of LTS, which when applied here, would yield a CC_{low} of 10% for LTS = 12 K and 24% for LTS = 14 K. However, CC_{low} observed near Barbados (Fig. 5h) exhibits a modest seasonality around a mean value of about 30%. Although cloudiness is observed to decrease from September to November as LTS decreases, its predictive skill is less evident when contrasting, for instance, February–March with June–July. The period June–July, namely, has a higher CC_{low} but a lower LTS. Here, the shift from a typical trade wind flow with large-scale subsiding motion to large-scale rising motion likely invalidates the conditions for which the LTS–CC_{low} relationship was found to hold. The RH in the cloud layer also shows a reverse relationship to CC_{low}, with the lowest values for CC_{low} during the more humid wet season. Parameters that more evidently follow the behavior of CC_{low} from winter to summer are the wind speed near the surface and the surface latent heat flux. The drier winter season experiences strong winds and large surface moisture fluxes, as well as large CC_{low}. Despite the larger SSTs during the wet season, the latent heat flux decreases toward the end of summer, following

the decrease in wind speed, and presumably the increase in RH. The sensible heat flux does not follow this pattern and remains at large values even during the period with lowest CC_{low} in September–October.

In section 4 we return to these parameters that may explain cloudiness on seasonal time scales. First, the behavior of cloudiness in terms of its amount and seasonality is evaluated in more detail. The BCO observations and the MODIS cloud record are compared for their coinciding time periods, and the influence of high cirrus clouds on the MODIS-derived low-level cloudiness, as well as the biases that are introduced when observing clouds at a single location at the BCO, are discussed. Furthermore, we address whether individual years have a similar seasonal cycle, as in the climatological mean, or whether significant interannual variability is present.

b. Cloudiness

To compare the seasonality in CC_{low} observed by MODIS with that at the BCO, the ceilometer-derived CC_{low} and lidar-derived CC_{high} are matched with the MODIS daytime overpasses for the period from April 2010 to April 2012. The BCO CC_{low} is derived over a time window starting at the MODIS overpass time and ending 20 h later, whereby 20 h is the approximate time period needed for an air mass to be advected across the $5° × 5°$ region at an average wind speed of $7\,m\,s^{-1}$. Days with near-surface westerly winds, based on ERA-Interim, are excluded.

The seasonality is plotted using 20-day averages of the above matching cloud estimates (Fig. 5g,h). We also compare 5-day means of CC_{low} and CC_{high} for months with $\omega_{700\_hPa} > 0$ (orange) and with $\omega_{700\_hPa} < 0$ (green) in Fig. 6. The seasonality is not sensitive to how we match the MODIS and BCO measurements: for instance, by changing the 20-h time window. However, absolute values of CC_{low} are sensitive, related to a nonnegligible diurnal cycle in cloudiness. Between 0600 and 0800 local time, cloudiness is about 10% higher than at noon, and about 5% higher than during the remainder of the day (not shown). Hence, MODIS cloudiness will be generally underestimated by only using their daytime overpasses. In Fig. 5 an underestimation of CC_{low} is apparent only for the dry season, which raises the question of whether this bias is due to the diurnal cycle in cloudiness being more pronounced in the dry season than in the wet season. However, a similar diurnal cycle is found in both seasons, and omitting the early morning hours from the BCO data does not change the seasonal cycle (not shown).

Despite being inherently different measurements in terms of resolution, detection thresholds, and field of view, the agreement between MODIS and BCO is
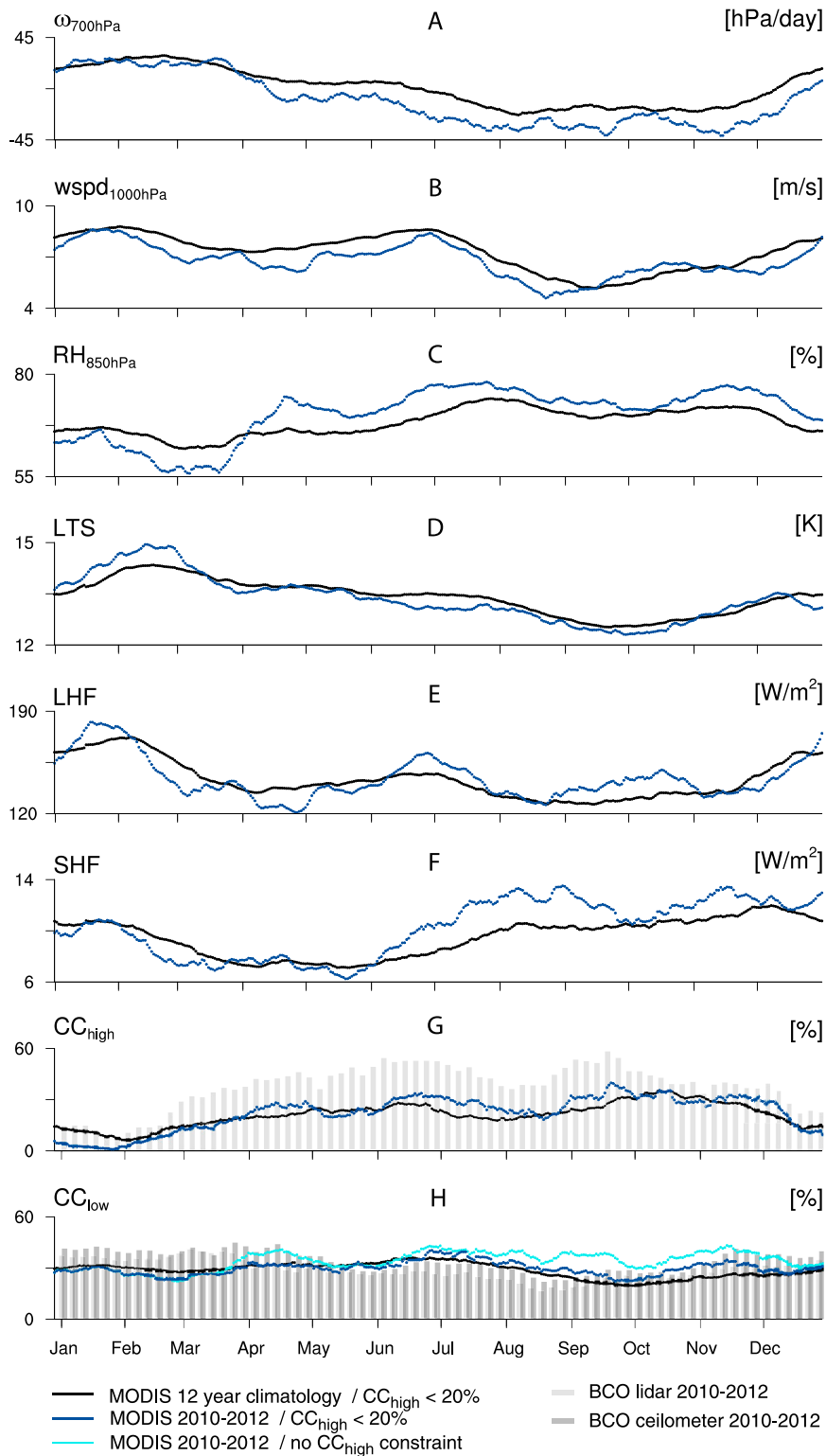
FIG. 5. Average seasonal cycle of 12 years (black) and a subset of 2010–12 (blue). (a)–(f) Commonly used parameters describing the large-scale flow and thermodynamic structure of the lower troposphere: (a) large-scale vertical velocity, (b) 1000-hPa wind speed, (c) relative humidity below the inversion at 850 hPa, (d) lower-tropospheric stability, and (e) surface sensible and (f) latent heat flux, all derived from ERA-Interim data. (g),(h) The seasonal cycle in (g) high-level cloud cover and (h) low-level cloud cover from MODIS daytime overpasses (blue: $CC_{high} < 20\%$; cyan: no CC_{high} condition).
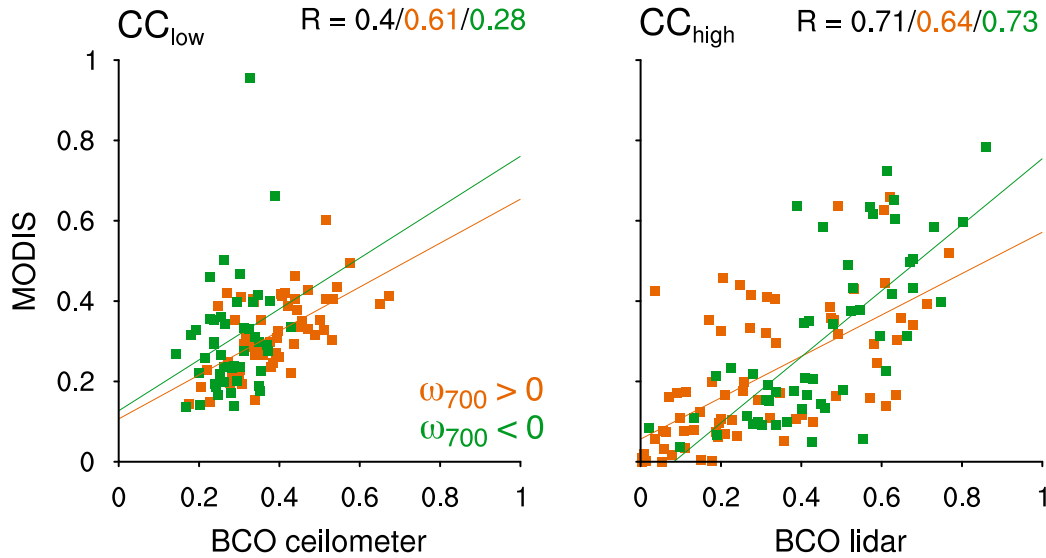
FIG. 6. The 5-day means of MODIS (left) CC_{low} and (right) CC_{high} are plotted against BCO CC_{low} and CC_{high} (100%) for the dry season ($\omega_{700\_hPa} > 0$; orange) and the wet season ($\omega_{700\_hPa} < 0$; green) separately. Linear regression lines and the Pearson correlation coefficients R that correspond to the dry (orange) and wet seasons (green) are shown separately.

surprisingly reasonable, even on a shorter 5-day time scale (Fig. 6). Both data sources agree that the seasonality in CC_{low} is relatively small (compared to, for example, the seasonality in CC_{high}), varying by about 10% around a mean value of 30% and rarely approaching values less than 10% or more than 40% (Fig. 5h) for the ceilometer (light gray bars) and MODIS (black line). As mentioned in the introduction, the relative invariance in CC_{low} has been attributed to the lack of seasonality in cloud found near the LCL (Nuijens et al. 2014), which contributes the larger part (two-thirds) to the total cloud cover. The relative invariance of this cloud component over longer time scales may be explained by the rapid adjustment of the subcloud layer to perturbations, which constrains the surface buoyancy and cumulus mass flux. In existing theories of shallow convection and in large-eddy simulation studies, the cumulus mass flux has been shown to act like a regulator or valve that constraints convection by keeping cloud-base height close to the mixed-layer top (Bretherton et al. 2004; Stevens 2006; Neggers et al. 2006; Bellon and Stevens 2013). Most of the seasonality in CC_{low} is therefore related to clouds farther aloft and, in particular, the presence of deeper cumuli (whose edges contribute to projected cloud cover) and of stratiform outflow layers at about 2 km, near the detrainment level of cumulus tops. Somewhat deeper cumuli and stratiform layers are more prevalent during the dry season (Nuijens et al. 2014), which seems counterintuitive, given that the wet summer season experiences mean rising motion, higher SSTs, and larger humidities. We hypothesize that the presence of deeper

convection leads to compensating downward motion in its surroundings, which limits shallow convection and cloudiness in the wet season overall.

The relative maxima in CC_{low} from January to May and the minima in CC_{low} from August to November are less pronounced in the MODIS than in the BCO record. Several explanations may be conceived beyond the seasonality in the diurnal cycle that was hypothesized earlier and was not found to explain the biases. First, a seasonality in the amount of probably cloudy pixels may exist, which is not captured by MODIS, because only their confidently cloudy pixels are used. However, the stratiform cloud layers that contribute to the larger CC_{low} in the BCO record during the dry season are relatively opaque (Nuijens et al. 2014), making it unlikely that these would fall into the probably cloudy category. Furthermore, the tenuous cloud that sits near the LCL (and which would fall into the probably cloudy category), has been found to be relatively invariant across seasons. Previous studies have also shown that the underestimation of cloudiness due to the small size and fragmented nature of cumuli, which fall below the detection threshold of the satellite sensor, is largely compensated for by the overestimation of cloudiness, because the signal gets smeared over pixels that are much larger than the individual size of a cloud (Zhao and Di Girolamo 2006). Second, an explanation may lie in the different fields of view of MODIS and BCO, whereby MODIS observes a larger area, which is also upstream of the BCO. During the time that it takes for an air mass to travel through that area (roughly a day),

the clouds further develop and deepen, especially if SSTs further increase. Such a deepening has been found to be accompanied by more lateral spreading of cloud near their tops, especially as subsidence is not strong enough to dry the layer at these heights (Nuijens and Stevens 2012). This potential may be larger in winter, when winds are stronger, surface fluxes are larger, and more wind shear is present (see also Fig. 9). Hence, at the downstream location of the BCO, the clouds may simply have changed their appearance compared to the larger MODIS area. The location is also closer to the South American coastline, over which deep convection during the wet season is common, which may affect shallow convection through an influence on the vertical velocity field. Third, clouds do not always pass a single location along their longest axes, so their length or equivalent size is generally underestimated compared to when viewed over a larger area (Rodts et al. 2003). However, if clouds tend to be more sheared in the direction of the wind during the dry season, this effect may be less pronounced, and the seasonality in cloudiness is somewhat more pronounced at a single location. Finally, an issue for passive satellite sensors is that the presence of high-level clouds can obscure underlying low-level clouds. Cirrus clouds seem to be an issue for the MODIS retrievals, because high-level cloud pixels are often surrounded by spurious low-level cloud pixels that raise CC_{low} (see the discussion in section 1). If scenes with $CC_{high} > 20\%$ would not have been excluded, indicated by the cyan line in Fig. 5h, the minimum in CC_{low} is less evident.

c. Interannual variability

The timeframe from 2010 to mid-2012, when the BCO measurements took place, exhibits stronger rising motion throughout the wet season compared to the 12-yr climatology, indicated in Fig. 7a, which shows the monthly-mean values for each separate year. Not only during 2010 and 2011, but also during 2005 (the year that the RICO campaign took place), the anomalous rising large-scale motion is accompanied by higher SSTs and weaker, more southerly, winds. These changes are consistent with a northward displacement of the ITCZ and a weakening of the North Atlantic subtropical high. The apparent slowdown of the circulation during these years may be a remote ENSO response (Enfield and Mayer 1997). There is also a hint of a higher RH during these periods, but an ad hoc relationship between RH and CC_{low} is not visible.

CC_{low}, in a given month, behaves very differently across years. For instance, July 2005 has anomalies in CC_{low} of up to -10%, whereas July 2010 has anomalies of $+10\%$, even though both months occur in years that

have similarly large anomalies in ω_{700_hPa} and SST (Fig. 7). This hints that CC_{low} has a subtle response to changes in many different parameters. Another example of how one parameter is not a single good predictor of CC_{low} can be seen from LTS in February and March 2010. This period has the highest positive anomaly in LTS, as southerly flow advects very warm air into the region. However, the effect of a higher LTS is counteracted by the effect of a large negative anomaly in RH, and, perhaps as a result, CC_{low} is low. There is no corresponding large anomaly in ω_{700_hPa}, which hints that LTS and RH are instead controlled by the magnitude of ω upstream, which emphasizes that the airmass history plays an important role in controlling cloud variations.

Figure 7 also illustrates that certain parameters are more prone to variability during a certain season, quantified by the standard deviation that is shown as a black line above each panel. Most notable are the larger variabilities in LTS and RH from January to May, whereas ω_{700_hPa} has a larger variability from May to August and at the end of November. Small changes in the circulation and origin of air masses during the dry season, when stronger easterly trade winds prevail, apparently have large effects on the stability and RH in the boundary layer. This sensitivity is smaller during the wet season, even though synoptic disturbances, which are averaged out in these monthly data, during that season are more common. We also note that interannual variability in CC_{low} is most pronounced from April to July, which is also the period during which variations in the North Atlantic subtropical high play a role (Fig. 7i).

4. Seasonal and synoptic time-scale controls on low-level cloudiness

a. Seasonal controls

From Fig. 5h, we have seen that during the dry season CC_{low} is, on average, 30%, whereas toward the end of the wet season, a somewhat lower CC_{low} of about 20% is observed. In this section, the relationships that may drive the changes in cloudiness from one month to the next are explored by means of a correlation analysis, which targets relationships on monthly time scales. Figure 8 shows correlation coefficients between CC_{low} and several parameters (to the right of the diagonal), as well as their scatterplots (to the left of the diagonal). The correlation coefficients are calculated on 31-day running averages from which the encompassing 365-day running average is subtracted. This removes the influence of interannual variability (Fig. 7), leaving only monthly or seasonal variability. The scatterplots are colored by the actual ω_{700_hPa} of each month (e.g., not of the ω anomaly). When
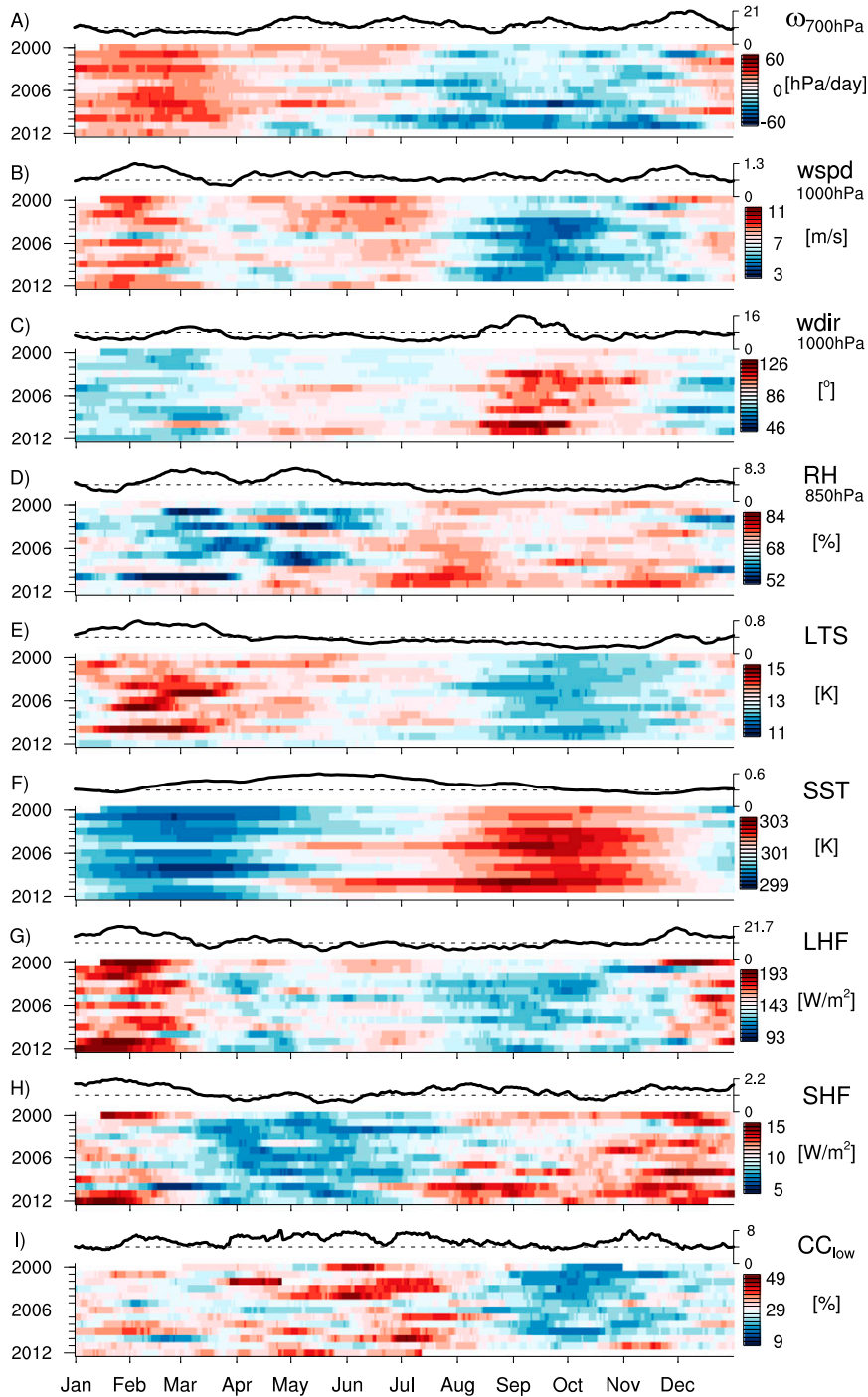
FIG. 7. Interannual variability of monthly means for MODIS and ERA-Interim data between 2000 and mid-2012. Above each contour plot, a black line shows the standard deviation of a particular month across the 12 years, which allows us to quantify the variability throughout the year.

correlations are not significant ($\alpha = 99.9\%$), they are not shown. Although the correlation analysis does not reveal causality, it does hint at those parameters that play an important role, either alone or through covariations with other parameters. With the help of existing knowledge of what drives the trade wind boundary layer, the largest correlations may be interpreted. Because of the shift from a regime with mean subsiding motion, to one with mean
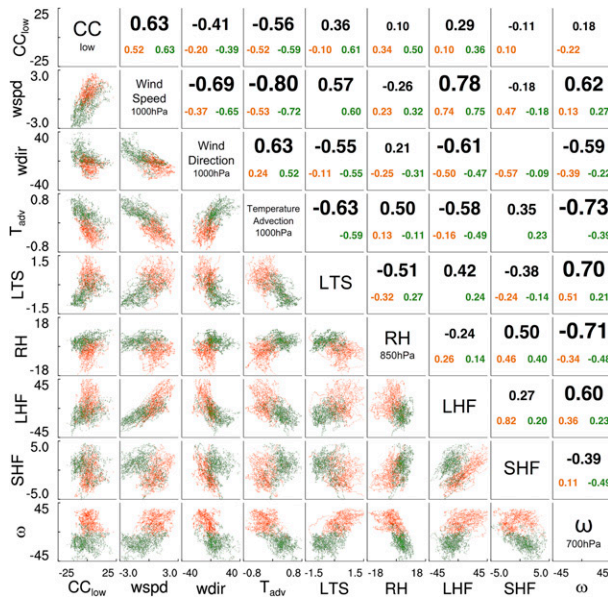
FIG. 8. Seasonal correlation coefficients between monthly-mean MODIS CC_{low} anomalies and monthly-mean anomalies of ERA-Interim: 1000-hPa wind speed ($m\,s^{-1}$), 1000-hPa wind direction (°), temperature advection ($K\,day^{-1}$), LTS (K), relative humidity at 850 hPa (%), the surface LHF, the surface SHF, and 700-hPa ω ($hPa\,day^{-1}$). Anomalies are with respect to the yearly mean (31-day running averages minus their encompassing 365-day running average), which removes interannual variability and targets relationships on seasonal time scales. Data are from 2000 to mid-2012. Positive wind direction anomalies correspond to a clockwise shift. Left of and below the diagonal are scatterplots of the respective variable pair, colored by $\omega_{700\_hPa} > 0$ in orange and $\omega_{700\_hPa} < 0$ in green, where ω is the actual monthly-mean value. Right of and above the diagonal are the Pearson correlation coefficients for the respective variable pair (black font sizes scaled by correlation magnitude). Black numbers for both seasons, orange numbers are for dry winter ($\omega_{700\_hPa} > 0$) season, and green numbers are for wet summer ($\omega_{700\_hPa} < 0$) season. Missing correlations are not significant ($\alpha = 99.9\%$).

rising motion, we also calculate correlations separately for each season, which are shown in orange and green below the overall correlation coefficient.

We find that the overall correlations of wind speed, wind direction, and temperature advection with CC_{low} have a similar sign and magnitude within each individual season. The correlations of CC_{low} with LTS, RH, and surface fluxes, however, which are more strongly influenced by the vertical velocity ω_{700_hPa}, can change sign as well as magnitude when considered for each individual season, similar to ω_{700_hPa} itself. These parameters also have smaller correlations than the winds and temperature advection. Furthermore, all correlations, except those of ω_{700_hPa}, are stronger during the wet season than during the dry season. In other words, CC_{low} appears more sensitive to variations in the large-scale

flow in a regime with mean rising motion than in a regime with mean subsiding motion.

The correlation of CC_{low} with ω_{700_hPa} is thus poor ($r = 0.18$), even though the season with the climatologically strongest subsiding motion has more low-level clouds than the season with the climatologically strongest rising motion (Figs. 5a,h). Within the regime of $\omega_{700\_hPa} > 0$ (orange) the correlations are reversed ($r = -0.22$; Fig. 8), which implies that within the dry winter season, those months that have somewhat less subsidence experience larger CC_{low}. This is also evident in Fig. 9a, which shows mean profiles of ω that are conditioned on season and on CC_{low}. Note that we added the overall mean profile to each anomaly profile just to make a comparison easier. This relationship presumably reflects that reduced downward motion leads to a deepening of clouds and the boundary layer. The conditional profiles suggest that this is also true within the wet season: an increase in mean rising motion leads to larger CC_{low}. Because clouds are irregularly shaped and often sheared, the deepening of clouds by itself acts to increase the projected cloud cover (Nuijens and Stevens 2012). Deeper clouds are also likely to live longer, which also increases CC_{low}. A similar relationship is seen between the BCO-derived CC_{low} and ω_{700_hPa} from the ECMWF IFS in Fig. 10, but only for the wet season. Because the ω_{700_hPa} is the least-constrained variable in the IFS, and only 2 years of data are used, we do not place much trust into this particular result.

Similarly to ω_{700_hPa}, the correlation between CC_{low} and RH is weak overall, because the dry season supports more cloud than the wet season (Fig. 8 and the profiles in Figs. 9e and 10e). However, within each season, small increases in RH may increase cloudiness. The correlation between CC_{low} and LTS is stronger ($r = 0.36$), reflecting that the winter season with increased ω_{700_hPa} and a larger stability supports more cloudiness. This is also seen from Figs. 9d and 10d, wherein the gradients in virtual potential temperature near 850–800 hPa strengthen. This reminds one of the Klein and Hartmann (1993) relationship and may reflect that increased stability promotes the lateral spreading of clouds just underneath the inversion, near the detrainment level of cumulus tops. It is somewhat puzzling that this relationship holds for the wet season but not for the dry season. One idea may be that the increased stability is a necessary but not a controlling factor for cloudiness, especially not when it is already sufficiently large. A further increase in inversion strength may thus further limit cloudiness, because it increases the entrainment of relatively drier and warmer air, which, especially near cumulus tops, may inhibit the persistence of detrained layers of cloud.
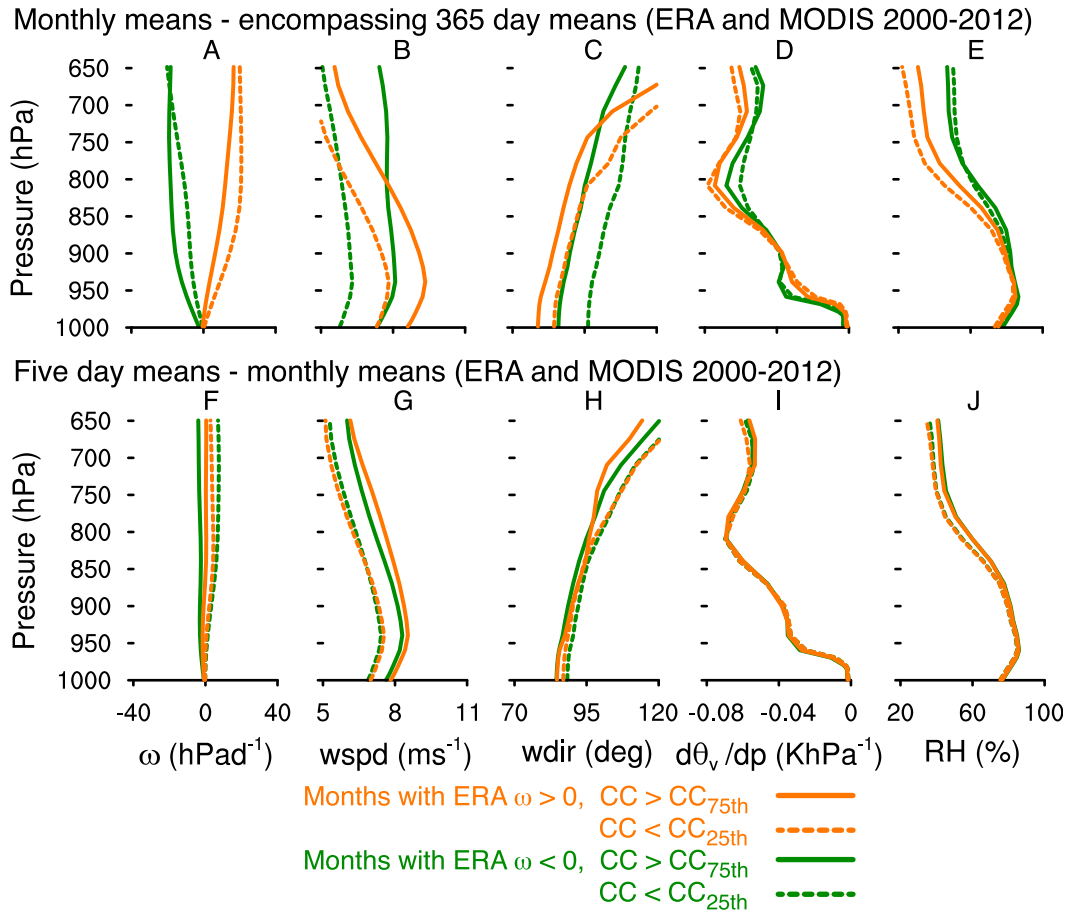
FIG. 9. Mean profiles for Barbados upstream area (2000–12) of (a),(f) ω, (b),(g) wind speed, (c),(h) wind direction, (d),(i) vertical gradient of virtual potential temperature, and (e),(j) RH, for the highest quartile (solid) and the lowest quartile (dashed) of MODIS CC_{low}. Further binning is based on dry season ($\omega_{700\_hPa} > 0$; orange) and the wet season ($\omega_{700\_hPa} < 0$; green). Data are from ERA-Interim. (top) Profiles are based on the monthly minus the yearly means to target seasonal variations. (bottom) Profiles are based on 5-day means minus monthly means to target synoptic variations. The mean profile was added to the conditionally averaged anomalies to illustrate differences in the vertical structure.

The correlation between LTS and RH is negative in the dry season and negative when both seasons are combined (Fig. 8). This likely reflects the fact that both parameters are strongly, but oppositely, correlated with ω_{700_hPa}. An increase in ω_{700_hPa} will increase the stability but will also dry the boundary layer more. Similar to what Myers and Norris (2013) found for stratocumulus, the increased stability may increase cloudiness, but the increased drying may decrease cloudiness. These opposing effects may contribute to both parameters having much smaller correlations with CC_{low} overall.

Returning to the correlation matrix (Fig. 8), we find that near-surface wind speed, followed by temperature advection and wind direction, have the strongest correlations with CC_{low}. This is also true within each season individually, although LTS and RH have caught up with

wind speed in the wet season (only). We note that the correlation coefficients for advection and LTS have a similar magnitude, as was found in the transition region by Klein (1997). The correlation with wind speed is further supported by the conditional profiles in Figs. 9 and 10 and may reflect different processes. First, wind speed also correlates well with wind direction ($r = -0.69$) and with temperature advection ($r = -0.8$) and may thus reflect the importance of the airmass origin, such as the amount of subsidence that is experienced upstream, or how cold the air mass is (Mauger and Norris 2010). Second, wind speed covaries with wind shear across seasons (Figs. 9 and 10), whereby shear increases the projected cloud cover (Hinkelman et al. 2007). However, shear itself only has a small correlation with CC_{low} ($r = 0.14$, not shown). Third, stronger winds
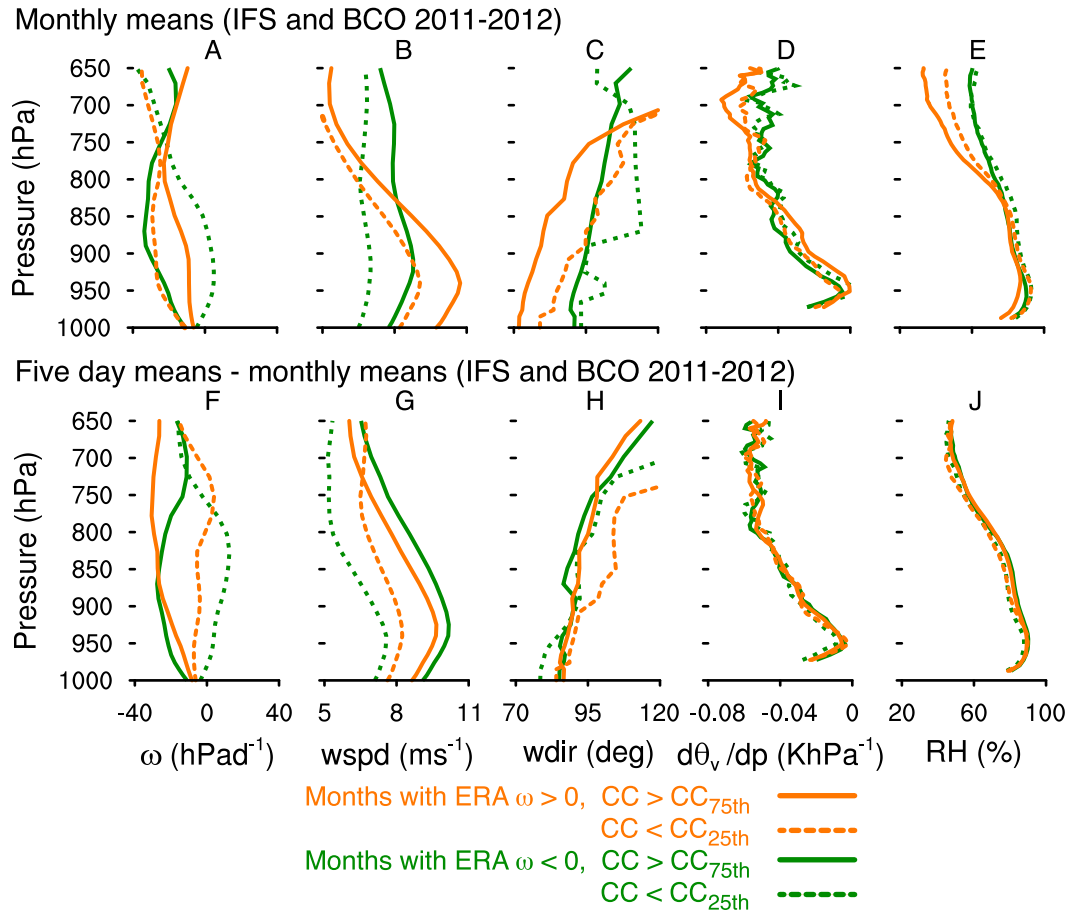
FIG. 10. Mean profiles for BCO area (2011–12) of the same variables as in Fig. 9, but CC_{low} binning based on BCO ceilometer and data from ECMWF IFS (ω, wind speed, and wind direction) and BCO (θ_v gradient and RH). (a)–(e) Profiles are based on monthly means to target seasonal variations. No yearly mean is subtracted, because interannual variability is small. (f)–(j) Profiles are based on 5-day means minus monthly means to target synoptic variations. The mean profile was added to the conditionally averaged anomalies to illustrate differences in the vertical structure.

deepen clouds and the boundary layer, which also increases projected cloud cover (Nuijens and Stevens 2012). The latter may be the most important mechanism, given that the correlation between wind speed and CC_{low} is stronger than that of wind direction or temperature advection with CC_{low} alone.

Using LES and bulk theory, the deepening of the cloud layer with a strengthening of the winds has been found to be a necessary part of the adjustment of the trade wind layer to a new equilibrium, to resolve an imbalance in the subcloud layer. The adjustment toward a deeper cloud layer is accomplished by the transient response of the cumulus mass flux, which initially increases with wind speed, effectively transporting much more moisture to the upper part of the cloud layer. As the boundary layer and clouds deepen, the cloud cover increases, both through an increase in projected area, and through the formation of stratiform outflow near

cumulus tops. As the deepening brings drier and warmer air to the surface, a large input of moisture at the surface can be maintained, but, at the same time, it reduces the surface sensible heat fluxes (in LES). Over the course of a couple of days, the surface fluxes can relax back in their adjustment to a new equilibrium, which may no longer reflect the initial transient response (Nuijens and Stevens 2012).

It is questionable whether the small correlations found between CC_{low} and the latent and sensible heat fluxes in Fig. 8 reflect such processes, given that the model may not accurately reproduce such interactions between convection and the large-scale flow. It is, for instance, somewhat puzzling that the latent heat flux correlates significantly better with wind speed, wind direction, and temperature advection than the sensible heat flux does. Despite the correlation with wind speed, cloudiness, however, does not correlate well with the

surface moisture flux. This supports the idea that the deepening of the layer arises just from an increase in the wind speed, as suggested from LES, which may increase cloudiness regardless of the further adjustment of the surface fluxes.

b. Synoptic controls

When turning to synoptic (5-day) time scales, from which the seasonality is removed, we observe that most correlations significantly drop. Several correlations also become insignificant, and separating them by season makes a smaller difference (Fig. 11). For the transition region, Klein (1997) found a much smaller decrease of the correlation coefficients of the most important parameters when removing monthly means. This suggests that trade wind cumulus may be harder to predict than stratocumulus, using parameters that represent the large-scale flow.

The largest correlations with CC_{low} still include that of wind speed but also include RH and the sensible heat flux. Similarly, in the conditional profiles (Figs. 9i,j and 10i,j) the only discernible differences are seen in the wind speed profiles, while differences in the θ_v gradients and RH have become much less evident. Whereas the wind speed still has a small but significant correlation with CC_{low} ($r = 0.24$), the wind direction and temperature advection no longer do, despite the fact that the wind speed and the temperature advection are still correlated. This reinforces the idea that the wind speed not only relates to cloudiness because of its covariance with the direction of the wind and the properties of the air mass, but also through its direct influence on boundary layer and cloud depth. We also note that the correlations between the sensible heat flux and the wind speed and temperature advection are, in fact, much larger on these shorter time scales than on monthly time scales. In addition, the correlation with CC_{low} has increased. This is an interesting result, because it would support the idea that, over longer time scales, the further adjustment of the surface fluxes hides their effect on cloudiness, which does play a role on shorter time scales.

One may have expected that the correlation with RH would have been much better, because, by definition, clouds imply 100% RH. One explanation may be that the reanalysis does not adequately represent the heterogeneity in the humidity field, which is observed to be rich (Siebert et al. 2013), and RH, when averaged over a larger area or over longer time scales, is a poor reflection of the local humidity variations that drive CC_{low}.

5. Conclusions

The region upstream of the island of Barbados (10.5°–15.5°N, 54°–59°W) is an interesting region from a climate
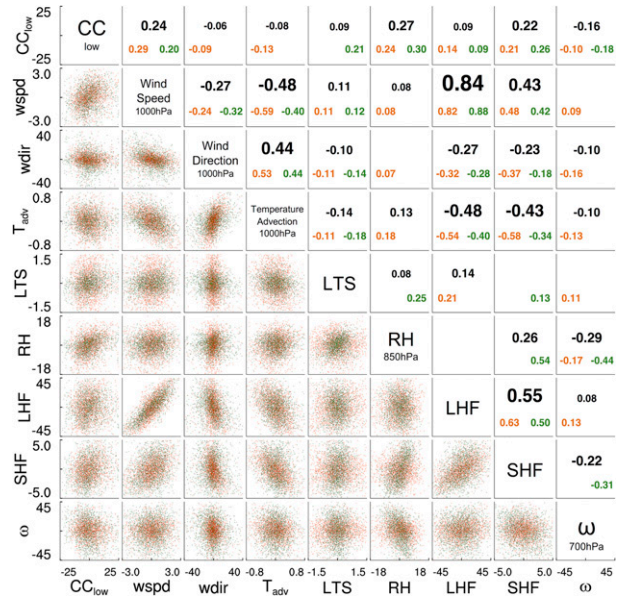

FIG. 11. Synoptic correlation coefficients between 5-day-mean MODIS CC_{low} anomalies and 5-day-mean anomalies of ERA-Interim. Anomalies are with respect to the 31-day mean (5–31-day average), which removes seasonal variability and targets relationships on synoptic time scales. Data are from 2000 to mid-2012. Parameters and seasonal binning are equal to Fig. 8.

modeling point of view, because it experiences two seasons with a distinct meteorology but with a mean low-level cloud amount (CC_{low}) that is relatively robust. Data from 12 years of ERA-Interim show that, during boreal winter, the region experiences trade wind–like conditions, with moderate large-scale subsiding motion of about 20 hPa day^{-1} from December to May, as well as strong surface winds from the east–northeast. These bring air masses with a moderate LTS of about 13–14 K. During boreal summer, from June to November, the region instead experiences mean moderately rising motion at −20 hPa day^{-1}, as the region is located on the northern edge of the ITCZ. The winds are weaker from the east–southeast, and RH in the upper boundary layer is about 20% higher than during winter. The LTS is only decreased by about 1 K.

In both the MODIS climatology of cloudiness over the same region and the data record from vertical profiling instruments at the Barbados Cloud Observatory (BCO), CC_{low} exhibits a small seasonality around a mean value of 30%, with the largest CC_{low} during winter and the smallest CC_{low} during late summer, from August to November. The seasonality in MODIS is less pronounced than at the BCO, in terms of a less-pronounced maximum of CC_{low} in winter, as well as a less-pronounced minimum in late summer. The first point may be attributed to the different field of views of

the instruments, whereby the BCO measures a single location that is downstream of the area over which cloudiness from MODIS is derived. Over the course of a day, as air masses travel across this region toward the BCO, clouds may further deepen and develop. A deepening of the cloud field more generally is hypothesized to be a major factor in explaining the larger CC_{low} during winter. A preceding study using the BCO record found that the winter not only had larger CC_{low}, but also relatively deeper cumuli accompanied by stratiform outflow near their tops (Nuijens et al. 2014). Both the deepening and the stratiform outflow would lead to a larger projected cloud cover, and especially when aligned in the direction of the wind, with a larger wind shear in winter, such an effect may be more pronounced at the downwind BCO site (relative to the MODIS area).

The second discrepancy in the less-pronounced summer minimum in MODIS may relate to the strong seasonality in high-level cloud CC_{high}, which is much larger during summer than winter. In MODIS images, high-level clouds are often surrounded by arbitrary low-level cloud pixels, which may be the result of a poor performance of CO_2 slicing methods in cases of broken cloud fields, whose effect is to decrease the apparent cloud-top height. Excluding scenes in which CC_{high} is more than 20% brings the two observational datasets closer to each other.

Monthly-mean CC_{low} is found to correlate most strongly with the surface wind speed, followed by temperature advection and wind direction. The fact that the wind speed has the strongest correlation with cloudiness suggests that it may affect clouds in a more direct way than just through its covariance with the origin of the air masses (wind direction), the temperature of the air masses (temperature advection), and wind shear, which itself has only a small correlation with CC_{low}. The strengthening of the winds has been found to lead to a deepening of the cloud layer and thus a deepening of the boundary layer in LES (Nuijens and Stevens 2012). Using those simulations and bulk theory, the deepening response is found to be a necessary response of the trade wind layer to resolve an inconsistency in the subcloud layer in its adjustment to a new equilibrium. As clouds deepen under wind shear, their projected cloud cover is increased. In addition, as the inversion height and cloud-top height are raised to levels where large-scale drying due to subsidence is insufficient, the moisture transported to those levels may form extended layers of cloud just underneath the inversion. These will also help increase cloudiness and have been found to be the major mode of variability on longer time scales (Nuijens et al. 2014).

The lower-tropospheric stability (LTS) and surface latent heat flux have somewhat smaller correlations with CC_{low} compared to the winds and advection, followed by almost negligible correlations of the vertical velocity ω_{700_hPa} and relative humidity (RH) with CC_{low}. However, the correlation of LTS with CC_{low}, and to a lesser extent those of RH and the latent heat flux with CC_{low}, increases by a significant amount when considering only the summer season with conditions of mean rising motion. The fact that during the summer any additional increase in LTS more strongly covaries with an increase in cloudiness than during winter, which on average has larger LTS, suggests that LTS is a necessary ingredient for large CC_{low} but not a strong controlling factor of CC_{low}.

What may contribute to the relatively small correlation of ω_{700_hPa}, RH, and LTS with CC_{low}, compared to the winds, is that both RH and LTS correlate with ω_{700_hPa}, but with opposing signs. Larger ω_{700_hPa} corresponds to an increased inversion strength (LTS) and presumably a larger CC_{low}, but it also corresponds to a drier cloud layer (smaller RH) and presumably a smaller CC_{low}. These opposing effects have also been found to play a role in regions of climatologically higher LTS that are dominated by stratocumulus (Myers and Norris 2013).

When seasonality is excluded and much shorter time scales are considered (5 days), most correlations significantly decrease by a larger extent than what was found in Klein (1997). Hence, the covariability of, for instance, wind speed and temperature advection, or wind speed and LTS, appear to be important for trade wind cloudiness, which emphasizes that (changing) large-scale flow patterns need to be considered (e.g., in climate modeling studies) and that relating CC_{low} to just one parameter, for instance LTS, can be misleading. Small but significant correlations between CC_{low} and wind speed, RH, and ω_{700_hPa} remain on short time scales. Such factors have been shown to play a role in regulating deep convection as well (Back and Bretherton 2005), which suggests that trade wind cumuli may exhibit more similarities to the deep convection regime than to the stratocumulus regime. The absence of a single strong predictor of CC_{low} challenges the development of cloud parameterizations, especially those that need to be effective on daily time scales (for instance, in numerical weather prediction). Finally, our results emphasize that attempts to correct for meteorology in studies focusing on aerosol effects on clouds using a single measure, such as the RH, will largely fail in doing so.

processing. He also thanks Katrin Lonitz, Jörg Burdanowitz, and Malte Rieck for very productive discussions. The authors acknowledge MODIS and ECMWF for providing data. We acknowledge three anonymous reviewers for their constructive and insightful comments.

REFERENCES

Ackerman, S., R. Holz, R. Frey, E. Eloranta, B. Maddux, and M. McGill, 2008: Cloud detection with MODIS. Part II: Validation. *J. Atmos. Oceanic Technol.,* **25,** 1073–1086, doi:10.1175/2007JTECHA1053.1.

Back, L. E., and C. S. Bretherton, 2005: The relationship between wind speed and precipitation in the Pacific ITCZ. *J. Climate,* **18,** 4317–4328, doi:10.1175/JCLI3519.1.

Bellon, G., and B. Stevens, 2013: Time scales of the trade wind boundary layer adjustment. *J. Atmos. Sci.,* **70,** 1071–1083, doi:10.1175/JAS-D-12-0219.1.

Bony, S., and J. Dufresne, 2005: Marine boundary layer clouds at the heart of tropical cloud feedback uncertainties in climate models. *Geophys. Res. Lett.,* **32,** L20806, doi:10.1029/2005GL023851.

Boucher, O., and Coauthors, 2013: Clouds and aerosols. *Climate Change 2013: The Physical Science Basis,* T. F. Stocker et al., Eds., Cambridge University Press, 571–657. [Available online at http://www.climatechange2013.org/images/report/WG1AR5_Chapter07_FINAL.pdf.]

Bretherton, C., and R. Pincus, 1995: Cloudiness and marine boundary layer dynamics in the ASTEX Lagrangian experiments. Part I: Synoptic setting and vertical structure. *J. Atmos. Sci.,* **52,** 2707–2723, doi:10.1175/1520-0469(1995)052<2707:CAMBLD>2.0.CO;2.

——, and M. Wyant, 1997: Moisture transport, lower-tropospheric stability, and decoupling of cloud-topped boundary layers. *J. Atmos. Sci.,* **54,** 148–167, doi:10.1175/1520-0469(1997)054<0148:MTLTSA>2.0.CO;2.

——, J. McCaa, and H. Grenier, 2004: A new parameterization for shallow cumulus convection and its application to marine subtropical cloud-topped boundary layers. Part I: Description and 1D results. *Mon. Wea. Rev.,* **132,** 864–882, doi:10.1175/1520-0493(2004)132<0864:ANPFSC>2.0.CO;2.

——, P. Blossey, and C. Jones, 2013: Mechanisms of marine low cloud sensitivity to idealized climate perturbations: A single-LES exploration extending the CGILS cases. *J. Adv. Model. Earth Syst.,* **5,** 316–337, doi:10.1002/jame.20019.

Enfield, D., and D. Mayer, 1997: Tropical Atlantic sea surface temperature variability and its relation to El Niño–Southern Oscillation. *J. Geophys. Res.,* **102,** 929–945, doi:10.1029/96JC03296.

Fennig, K., A. Andersson, S. Bakan, C.-P. Klepp, and M. Schröder, 2012: Hamburg Ocean Atmosphere Parameters and Fluxes from Satellite Data—HOAPS 3.2—Monthly means/6-hourly composites. EUMETSAT CM SAF. doi:10.5676/EUM_SAF_CM/HOAPS/V001.

Frey, R., S. Ackerman, Y. Liu, K. Strabala, H. Zhang, J. Key, and X. Wang, 2008: Cloud detection with MODIS. Part I: Improvements in the MODIS cloud mask for Collection 5. *J. Atmos. Oceanic Technol.,* **25,** 1057–1072, doi:10.1175/2008JTECHA1052.1.

Hartmann, D., M. Ockert-Bell, and M. Michelsen, 1992: The effect of cloud type on Earth's energy balance: Global analysis. *J. Climate,* **5,** 1281–1304, doi:10.1175/1520-0442(1992)005<1281:TEOCTO>2.0.CO;2.

Hinkelman, L., K. Evans, E. Clothiaux, T. Ackerman, and P. Stackhouse Jr., 2007: The effect of cumulus cloud field anisotropy on domain-averaged solar fluxes and atmospheric heating rates. *J. Atmos. Sci.,* **64,** 3499–3520, doi:10.1175/JAS4032.1.

Karlsson, J., G. Svensson, S. Cardoso, J. Teixeira, and S. Paradise, 2010: Subtropical cloud-regime transitions: Boundary layer depth and cloud-top height evolution in models and observations. *J. Appl. Meteor. Climatol.,* **49,** 1845–1858, doi:10.1175/2010JAMC2338.1.

Kelly, P., and B. Mapes, 2011: Zonal mean wind, the Indian monsoon, and July drying in the western Atlantic subtropics. *J. Geophys. Res.,* **116,** D00Q07, doi:10.1029/2010JD015405.

King, M., and Coauthors, 2003: Cloud and aerosol properties, precipitable water, and profiles of temperature and water vapor from MODIS. *IEEE Trans. Geosci. Remote Sens.,* **41,** 442–458, doi:10.1109/TGRS.2002.808226.

Klein, S., 1997: Synoptic variability of low-cloud properties and meteorological parameters in the subtropical trade wind boundary layer. *J. Climate,* **10,** 2018–2039, doi:10.1175/1520-0442(1997)010<2018:SVOLCP>2.0.CO;2.

——, and D. Hartmann, 1993: The seasonal cycle of low stratiform clouds. *J. Climate,* **6,** 1587–1606, doi:10.1175/1520-0442(1993)006<1587:TSCOLS>2.0.CO;2.

——, ——, and J. Norris, 1995: On the relationships among low-cloud structure, sea surface temperature, and atmospheric circulation in the summertime northeast Pacific. *J. Climate,* **8,** 1140–1155, doi:10.1175/1520-0442(1995)008<1140:OTRALC>2.0.CO;2.

Köhler, M., 2005: Improved prediction of boundary layer clouds. *ECMWF Newsletter,* No. 104, ECMWF, Reading, United Kingdom, 18–22.

Li, Y., D. Thompson, G. Stephens, and S. Bony, 2014: A global survey of the instantaneous linkages between cloud vertical structure and large-scale climate. *J. Geophys. Res. Atmos.,* **119,** 3770–3792, doi:10.1002/2013JD020669.

Mauger, G. S., and J. R. Norris, 2010: Assessing the impact of meteorological history on subtropical cloud fraction. *J. Climate,* **23,** 2926–2940, doi:10.1175/2010JCLI3272.1.

Medeiros, B., and B. Stevens, 2011: Revealing differences in GCM representations of low clouds. *Climate Dyn.,* **36,** 385–399, doi:10.1007/s00382-009-0694-5.

Menzel, W., W. Smith, and T. Stewart, 1983: Improved cloud motion wind vector and altitude assignment using VAS. *J. Climate Appl. Meteor.,* **22,** 377–384, doi:10.1175/1520-0450(1983)022<0377:ICMWVA>2.0.CO;2.

Muñoz, E., A. Busalacchi, S. Nigam, and A. Ruiz-Barradas, 2008: Winter and summer structure of the Caribbean low-level jet. *J. Climate,* **21,** 1260–1276, doi:10.1175/2007JCLI1855.1.

Myers, T., and J. Norris, 2013: Observational evidence that enhanced subsidence reduces subtropical marine boundary layer cloudiness. *J. Climate,* **26,** 7507–7524, doi:10.1175/JCLI-D-12-00736.1.

Neggers, R., B. Stevens, and J. D. Neelin, 2006: A simple equilibrium model for shallow-cumulus-topped mixed layers. *Theor. Comput. Fluid Dyn.,* **20,** 305–322, doi:10.1007/s00162-006-0030-1.

Nuijens, L., and B. Stevens, 2012: The influence of wind speed on shallow marine cumulus convection. *J. Atmos. Sci.,* **69,** 168–184, doi:10.1175/JAS-D-11-02.1.

——, I. Serikov, L. Hirsch, K. Lonitz, and B. Stevens, 2014: The distribution and variability of low-level cloud in the North Atlantic trades. *Quart. J. Roy. Meteor. Soc.,* **140,** 2364–2374, doi:10.1002/qj.2307.

Platnick, S., M. King, S. Ackerman, W. Menzel, B. Baum, J. Riédi, and R. Frey, 2003: The MODIS cloud products: Algorithms

and examples from Terra. *IEEE Trans. Geosci. Remote Sens.,* **41,** 459–473, doi:10.1109/TGRS.2002.808301.

Rodts, S., P. Duynkerke, and H. Jonker, 2003: Size distributions and dynamical properties of shallow cumulus clouds from aircraft observations and satellite data. *J. Atmos. Sci.,* **60,** 1895–1912, doi:10.1175/1520-0469(2003)060<1895: SDADPO>2.0.CO;2.

Sandu, I., B. Stevens, and R. Pincus, 2010: On the transitions in marine boundary layer cloudiness. *Atmos. Chem. Phys.,* **10,** 2377–2391, doi:10.5194/acp-10-2377-2010.

Serikov, I., and S. Bobrovnikov, 2010: Atmospheric temperature profiling with pure rotational Raman lidars. *Recent Advances in Atmospheric Lidars,* L. Fiorani and V. Mitev, Eds., Optoelectronic Materials and Devices, Vol. 7, INOE, 149–216.

Siebert, H., and Coauthors, 2013: The fine-scale structure of the trade wind cumuli over Barbados — An introduction to the CARRIBA project. *Atmos. Chem. Phys.,* **13,** 10 061–10 077, doi:10.5194/acp-13-10061-2013.

Siebesma, A., and Coauthors, 2003: A large eddy simulation intercomparison study of shallow cumulus convection. *J. Atmos. Sci.,* **60,** 1201–1219, doi:10.1175/1520-0469(2003)60<1201: ALESIS>2.0.CO;2.

Simmons, A., S. Uppala, D. Dee, and S. Kobayashi, 2007: ERA-Interim: New ECMWF reanalysis products from 1989 onwards. *ECMWF Newsletter,* No. 110, ECMWF, Reading, United Kingdom, 25–35.

Slingo, J., 1987: The development and verification of a cloud prediction scheme for the ECMWF model. *Quart. J. Roy. Meteor. Soc.,* **113,** 899–927, doi:10.1002/qj.49711347710.

Small, R., S. de Szoeke, and S. Xie, 2007: The Central American midsummer drought: Regional aspects and large-scale forcing. *J. Climate,* **20,** 4853–4873, doi:10.1175/JCLI4261.1.

Stevens, B., 2005: Atmospheric moist convection. *Annu. Rev. Earth Planet. Sci.,* **33,** 605–643, doi:10.1146/ annurev.earth.33.092203.122658.

——, 2006: Bulk boundary-layer concepts for simplified models of tropical dynamics. *Theor. Comput. Fluid Dyn.,* **20,** 279–304, doi:10.1007/s00162-006-0032-z.

——, A. Beljaars, S. Bordoni, C. Holloway, M. Köhler, S. Krueger, V. Savic-Jovcic, and Y. Zhang, 2007: On the structure of the lower troposphere in the summertime stratocumulus regime of the northeast Pacific. *Mon. Wea. Rev.,* **135,** 985–1005, doi:10.1175/MWR3427.1.

Teixeira, J., and Coauthors, 2011: Tropical and subtropical cloud transitions in weather and climate prediction models: The GCSS/WGNE Pacific Cross-Section Intercomparison (GPCI). *J. Climate,* **24,** 5223–5256, doi:10.1175/2011JCLI3672.1.

Van Zanten, M., and Coauthors, 2011: Controls on precipitation and cloudiness in simulations of trade-wind cumulus as observed during RICO. *J. Adv. Model. Earth Syst.,* **3,** M06001, doi:10.1029/2011MS000056.

Vial, J., J. Dufresne, and S. Bony, 2013: On the interpretation of inter-model spread in CMIP5 climate sensitivity estimates. *Climate Dyn.,* **41,** 3339–3362, doi:10.1007/s00382-013-1725-9.

von Engeln, A., and J. Teixeira, 2013: A planetary boundary layer height climatology derived from ECMWF reanalysis data. *J. Climate,* **26,** 6575–6590, doi:10.1175/JCLI-D-12-00385.1.

Warren, S., C. Hahn, J. London, R. Chervin, and R. Jenne, 1988: Global distribution of total cloud cover and cloud type amounts over the ocean. NCAR Tech. Note NCAR/TN-317+STR, 43 pp., doi:10.2172/5415329.

Wood, R., and C. Bretherton, 2006: On the relationship between stratiform low cloud cover and lower-tropospheric stability. *J. Climate,* **19,** 6425–6432, doi:10.1175/JCLI3988.1.

Zhao, G., and L. Di Girolamo, 2006: Cloud fraction errors for trade wind cumuli from EOS-Terra instruments. *Geophys. Res. Lett.,* **33,** L20802, doi:10.1029/2006GL027088.